Cross-species permissivity: structure of a goat adeno-associated virus and its complex with the human receptor, AAVR.

Edward E. Large[1], Mark A. Silveria[1], Tommi A. White[2] and Michael S. Chapman[1]*

[1] Department of Biochemistry, University of Missouri, Columbia, MO 65201, USA; msilveria@mail.missouri.edu (M.A.S.); whiteto@missouri.edu (T.A.W.); largee@missouri.edu (E.E.L.); chapmanms@missouri.edu (M.S.C.)

[2] Current address: Bayer Crop Science, 700 W Chesterfield Pkwy W, Chesterfield, MO 63017 USA

* Correspondence: chapmanms@missouri.edu; Tel.: +1-573-882-9825

ABSTRACT

Adeno-associated virus (AAV) is a small ssDNA satellite virus of high interest (in recombinant form) as a safe and effective gene therapy vector. AAV's human cell entry receptor (AAVR) contains Polycystic Kidney Disease (PKD) domains bound by AAV. Seeking understanding of the spectrum of interactions, goat AAVGo.1 is investigated, because its host is the species most distant from human with reciprocal cross-species cell susceptibility. The structure of AAVGo.1, solved by cryo-EM to 2.9 Å resolution, is most similar to AAV5. Through ELISA studies, it is shown that AAVGo.1 binds to human AAVR (huAAVR) more strongly than do AAV2 or AAV5, and that it joins AAV5 in a class that binds exclusively to PKD domain 1 (PKD1), in contrast to other AAVs that interact primarily with PKD2. The AAVGo.1 cryo-EM structure of a complex with a PKD12 fragment of huAAVR at 2.4 Å resolution shows PKD1 bound with minimal change in virus structure, except for disordering of a neighboring surface loop. Only 4 of the 42 capsid protein sequence differences between AAVGo.1 and AAV5 occur at the PKD1 binding interface. These result in only minor conformational changes in AAVR, including a near rigid domain rotation with maximal displacement of the receptor by ~1 Å. A picture emerges of two classes of AAV with completely different modes of binding to the same AAVR receptor, but within each class atomic interactions are mostly conserved.

IMPORTANCE Adeno-Associated Virus (AAV) is a small ssDNA satellite parvovirus. As a recombinant vector with a protein shell encapsidating a transgene, recombinant AAV (rAAV) is a leading delivery vehicle for gene therapy with two FDA-

34 approved treatments and 150 clinical trials for 30 diseases. The human entry receptor
35 huAAVR has five PKD domains. To date, all serotypes, except AAV5, have interacted
36 primarily with the second PKD domain, PKD2. Goat is the AAV host most distant from
37 human with cross-species cell infectivity. AAVGo.1 is similar in structure to AAV5, the
38 two forming a class with a distinct mode of receptor-binding. Within the two classes,
39 binding interactions are mostly conserved, giving an indication of the latitude available
40 in modulating delivery vectors.
41
42 **KEYWORDS:** AAV5, AAVGo.1, AAVR, cell entry, virus receptor, gene therapy

INTRODUCTION

Adeno-associated viruses (AAVs) are small single-stranded DNA viruses that can be repurposed into effective and safe gene therapy delivery vehicles (1). Primate AAV serotypes are the dominant choice for gene therapy. Several structures have been determined, starting with that of AAV2 by X-ray crystallography (2). AAV coding regions consist of two major open reading frames (ORFs): *rep* and *cap*, encoding functions needed in viral replication/DNA packaging and the capsid protein respectively (3). The Cap ORF encodes phenotypes relevant in tissue tropism and immune recognition (4, 5).

AAV2 was instrumental in the discovery and characterization of a human proteinaceous AAV receptor (AAVR) (6) (Fig. 1B). AAVR is a glycoprotein (N-linked/O-linked) and contains three major protein regions. The N-terminus contains a Motif At N-terminus with Eight-Cysteines (MANEC) while the central extracellular portion contains five Polycystic Kidney Disease (PKD) domains numbered 1 to 5 from N-terminus to C-terminus (7). The C-terminus has a predicted transmembrane protein domain and cytosolic domain responsible for trafficking AAV through the trans-Golgi network (TGN) (6). Experiments in mouse models and human cell lines indicate the physical interactions between primate AAVs and AAVR receptors of different species can be conserved.

For human AAVR (huAAVR), structures for a handful of complexes are known (8-12). The structures consist of AAV1, AAV2 or AAV5 serotypes complexed with human PKD variants (huPKD) containing domains 1-2 (huPKD12) or domains 1-5 (huPKD15). Both structure and mutant data (13, 14) consistently indicate AAV5 is unlike all other AAVs whose interactions with huAAVR are mediated primarily through PKD2. Domain-

swap mutants show AAV5 interacting exclusively with PKD1 (13) and the cryo-EM structures of complexes with huAAVR fragments show that the PKD1 binding site on AAV5 (9, 11) is different from the common PKD2 site for AAV2 and AAV1 (8, 9, 11).

Domain-swap mutants indicate a secondary role for PKD1 with AAV2 and other serotypes (13) but multiple cryo-EM structures reveal only the tightly-bound PKD2 at high resolution (8, 12, 15) It seemed possible that AAV2-like viruses bound not just to PKD2, but also to PKD1, though so weakly that PKD1 had not been seen in the AAV2 structures. It was not as simple as overlaying PKD1 in an AAV5-like position and connecting it, as a single subunit chain, to PKD2 as found in AAV2, because connecting the domains required implausible stereochemistry (11).

AAV gene therapy utilizes primate serotypes of which AAV5 is currently the only known representative with primarily PKD1 interactions. AAV5 was initially isolated from a human penile lesion (Bantel-Schaal and Zur Hausen 1984) and is the sole primate AAV5 clade representative. The AAV5 clade also includes AAVGo.1 (16, 17), which was isolated from deceased neonatal goat ileum (Olson, Haskell et al. 2004). Both recombinant AAV5 and AAVGo.1 can transduce at equivalent levels in primate and ruminant cell lines (Arbetman, Lochrie et al. 2005, Qiu, Cheng et al. 2006). Efficient transduction of primate and ruminant cell lines by both AAV5 and AAVGo.1 represents the broadest divergence between AAV host species that are reciprocally permissive to cross-species infection. Given the strong evidence for AAV5 interactions with PKD1 we investigated potential interactions of AAVGo.1 with huAAVR.

Here, binding of AAVGo.1, AAV5 and AAV2 to domain combinations of huAAVR are compared by ELISA. Then high-resolution structures are determined by cryo-EM of

AAVGo.1 alone, and in complex with a PKD12 fragment of huAAVR. These are compared to corresponding structures of AAV5 to understand the diversity of interactions that are compatible with productive receptor-binding.

RESULTS

AAVGo.1 binds huAAVR.

HuAAVR binds to AAV5, AAVGo.1 and AAV2 with comparable order-of-magnitude avidities as measured by ELISA binding using huAAVR ectodomain constructs. In contrast to AAV2, the binding of both AAVGo.1 and AAV5 is mediated mostly through the PKD1 domain. Both have stronger overall binding avidity than AAV2, AAVGo.1 having the strongest yet measured (Figure 1).

Structure of AAV-Go.1 and its huAAVR receptor complex.

Cryo-EM single particle analysis (SPA) yielded reconstructions at 2.9 Å resolution for native AAVGo.1 and 2.5 Å for the AAVR PKD12 complex. Sharpened maps provided detail for atomic modeling and were interpretable from residue 209 to 726 of the capsid protein in both reconstructions with one exception. In the receptor complex, residues 477 to 482 are less ordered and only traceable in maps low-pass filtered to 10 Å resolution. By convention, the numbering of VP1 is used, even though it constitutes only 10% of the capsid subunits. The majority of the subunit common to VP1-3 is seen in the 60-fold averaged reconstructions, starting at residue 209, before βA. The N-terminus of VP3 is residue 193 by VP1 numbering, so the atomic model accounts for 517 of 534 (96.8%) VP3 residues.

The native AAVGo.1 capsid has a similar protein fold and surface topology to AAV5 structures (9, 11, 18). The capsid core, comprised of a jellyroll fold found in many virus structures (19), and a single α-helix (αA) are the most conserved features of AAVs, and AAVGo.1 is no exception. The AAVGo.1 core jellyroll has the standard topology with backbone chain alternating between two stacked antiparallel β- sheets (almost rolling into a single tube). The sheet forming the inner surface of the capsid consists of β-strands B, I, D and G that alternate with the "CHEF" strands of the outer sheet, together with a 5th inner strand, βA. βA is seen in many parvoviruses (20) at the edge of the BIDG sheet, running antiparallel to and turning directly into βB. Seven loops that connect strands of the BIDG and CHEF sheets encode much of the functionality of the capsid protein. Within the loops are regions of low sequence conservation that decorate the outer surface of the virus and these variable regions (VR) are enumerated as VR-I to VR-IX (21). VR-I (262-268) is found between βB and βC strands (BC loop), VR-II (362-330) is found in the DE loop, VR-III (380-388) is in the EF loop, VR-IV to VR-VIII (449-468, 487-504, 525-541, 544-556, and 579-594) are located in the GH loop and the C-terminus contains an additional VR-IX (704-711) after the last βI strand. These VR loops serve as guideposts for understanding AAV:AAVR interactions (8-12).

AAVGo.1 and AAV5 capsid proteins have high homology (94%). All 42 amino acid differences occurring in the VP3 region (more specifically C-terminal of AAVGo.1 VP1 residue 376) and the majority of these differences are located on the exterior of the capsid (17).

When comparing PKD1 as bound to AAVGo.1 or AAV5 we see an overall shift in the receptor position (Figure 3). Displacements of up to 1 Å are observed at some

backbone carbons (Figure 3B, C). The shift appears to be a rotation about Arg_{353} which remains essentially unmoved (Figure 3D). Displacements become greater with distance from Arg_{353}. What could cause this rotation between one serotype and another that are so similar? The key perhaps lies in the four residues that are changed in the binding footprint of AAVGo.1 when compared with AAV5.

The binding site formed by AAV5 and PKD1 has previously been examined (9, 11). Here, our attention is focused on the four viral residues within the binding interface that are different between AAVGo.1 and AAV5. Central to the binding site is human PKD1 residue Arg_{353}, which makes contact with AAV5 Ser_{531} and Gly_{545}. In AAVGo.1, the equivalent residues to Ser_{531} and Gly_{545} are, respectively, Ala_{533} and Asp_{547} (Figure 2C, D & Figure 4B, C). Both AAV5 Ser_{531} and AAVGo.1 Ala_{533} make contact (exclusively) with Arg_{353} (≤ 3.5 Å). AAVGo.1 Ala_{533} contacts AAVR Arg_{353} while the corresponding AAV5 Ser_{531} adds to the surface contact. Neighboring AAV5 Gly_{545} makes minimal contact with AAVR Arg_{353}, while the corresponding AAVGo.1 Asp_{547} makes several van der Waals contacts in addition to AAVR Arg_{353} (Figure 4B). In AAVGo.1 Pro_{545} replaces AAV5 Leu_{543} (Figure 2E, F & Figure 4D). Both are involved in somewhat different virus-receptor van der Waals contacts, probably of similar extents. Lastly, in AAVGo.1 Ser_{542} replaces AAV5 Ala_{540}, adding a hydroxyl group that forms a polar interaction with AAVR Asn_{395} (Figure 2E, F & Figure 4D). In summary, there are some detailed differences, the net effect of which is a modest increase in contacts and polar interactions for the AAVGo.1 complex compared to AAV5.

The largest difference, by sequence, is a double insertion in AAVGo.1 relative to the AAV5 sequence: L_{477}(SS)G_{478}. The region is disordered in AAVGo.1 receptor

complex, lacking density between Thr_{477} and Ser_{482} in the sharpened map. When low-pass filtered to 10 Å resolution, the backbone can be traced readily, indicating that the region is dynamic. In unbound AAV5 and AAVGo.1, this loop is not disordered, and it appears less disordered in the AAV5-AAVR complex. Thus, it does appear that the combination of receptor-binding and the tandem serine insertion increases the disorder. Indeed, the map recovered by low-pass filtering is close to the C-terminal end of PKD1, discussed below.

DISCUSSION

The largest difference in sequence between AAVGo.1 and AAV5 is the tandem serine insertion in variable region V (VR-V), a site that is more mobile than other regions of the surface, witness the fact that it is observed only in a lower resolution map low-pass filtered to 10 Å. The difference is within the epitope of a neutralizing monoclonal antibody, mAb HL2476 (22), and if the mAb were to be representative of natural neutralizing polyclonal antibodies, it is possible that the difference reflects selection through immune-evasion. We note that the loop that is extended in AAVGo.1 by the two-residue insertion is in the general vicinity of the final residue observed in PKD1, about 6 Å away, and one cannot exclude the possibility of an additional interaction between VR-V of AAVGo.1 and the interdomain linker between PKD1 and PKD2 in AAVR.

Prior to this work, most complexes between AAV and AAVR were of similar structure, like the AAV2 complex (8, 9, 12), with a single exception, that of AAV5 (9, 11). At first approximation, the binding of AAVGo.1 to huAAVR is similar to that of AAV5, so the single exception becomes a second class in terms of the mode of binding. Between

the two classes, the modes of binding are completely different. Within each class, the diversity in structure of the virus-receptor interface is much more modest. It is anticipated that within and between binding classes, diversity will yield distinct transduction efficiencies, tissue tropism and antibody neutralization profiles.

MATERIALS AND METHODS

Expression and purification of AAVGo.1 and AAVR constructs.

AAVGo.1, AAV2 and AAV5 Virus-Like Particles (VLPs) were produced using Sf9 cells and purified via ultracentrifugation in a cesium chloride gradient, repeated 4 times, and yielding a final concentration of 38.8 mg/ml (10). Sample purity and concentration were evaluated using nanodrop, SDS-PAGE and negatively stained electron microscopy using a JEOL JEM-1400 120kV Transmission Electron Microscope (TEM). AAVR fragment constructs (His_6PKD1; His_6PKD12; and His_6PKD15) were expressed and purified as previously described (10).

Enzyme-Linked Immunosorbent Assay (ELISA).

ELISA assays were carried out in triplicate using a modified direct ELISA protocol (6, 11). AAV2, AAV5, or AAVGo.1 VLPs (2.5 µg/ml) were incubated in ELISA plates (Corning Costar # 9018) in 100 mM NaHC03 (pH 9.6) and washed with TBST buffer (0.05% TWEEN in TBS). Plates were incubated with N-terminally His-tagged AAVR (His_6PKD1; His_6PKD12; or His_6PKD15) and detected with anti-6x His tag horseradish peroxidase (HRP) (abcam #ab1187) antibody. 3,3'5,5'-Tetramethylbenzidine (TMB) ELISA Substrate (abcam #ab171523) was added to each well and development was stopped using 1 M hydrochloric acid. The optical density of plates was evaluated at 450

nm using a microplate reader (BioTek Synergy H1 Hybrid Multi-Mode Reader). EC_{50} values were estimated using the ATT BioQuest® - EC50 calculator.

TEM/Single Particle Cryo-EM data acquisition and 3D image reconstruction.

Native AAVGo.1 and AAVGo1:PKD12 complexes were prepared and imaged as previously described for AAV2 and AAV5 (11, 12). Briefly, AAVGo.1 was dialyzed/diluted into HN buffer (25 mM HEPES pH 7.4 and 150 mM NaCl) at 0.33 mg/ml and PKD12 at 0.75 mg/ml. Grids had an ultrathin continuous carbon film layered on Lacey carbon supports (400 mesh; copper; Ted Pella # 01824). The grids were glow discharged using a PELCO easiGlow ™ Glow Discharge Cleaning System. After application of 2 µl of sample, native AAVGo.1 grids were blotted once and plunged directly into liquid ethane using an FEI Mark IV Vitrobot (force = 4, time = 2, temp = 25, humidity = 100). PKD12 complexes grids were prepared by adding 2 µl AAVGo.1 to the grid with a 2 minute incubation time. The grid was then wicked with Whatman filter paper (grade 595) and 2 µL of receptor was immediately added followed by blotting and plunging via Vitroblot (force = 4, time = 3, temp = 25, humidity = 100).

Cryo-EM grids were screened using an FEI Tecnai F30 Twin 300 kV TEM in preparation for single particle Cryo-EM. Native AAVGo.1 and AAVGo.1:PKD12 complexes were imaged using an FEI Titan Krios equipped with a Gatan K3 digital camera in super-resolution mode at a dose rate of 40 frames per 3.12 second exposure (Table 1). Automated micrograph data collection was enabled using Leginon (23).

Relion 3.1.0 was used to process the data for native AAVGo.1 (24). 713 micrographs were motion corrected using Relion's own implementation and CTFFind-4.1 was used for CTF correction (25). A total of 246,094 particles were picked with

Relion autopick, which were culled down to 188,650 through several rounds of 2D classification. An additional round of 3D classification resulted in 140,568 particles. 3D refinement produced a map of 3.62 Å (gold-standard $FSC_{0.143}$). Post-processing, including per particle CTF and motion corrections and masking resulted in a final resolution of 2.93 Å.

Relion 3.1.1 was used for the complex of AAVR PKD12 with AAVGo.1 (24). A total of 1204 micrographs were motion corrected with MOTIONCOR2 (26) and CTF estimation was carried out using CTFFind-4.1 (25). From 1127 micrographs, 208921 particles were picked using Relion's Autopick with the native AAVGo.1 structure as a template. 3D Refinement was carried out directly on the extracted particles and 3D classification was used with C1 symmetry imposed resulting in 71095 particles for 3D reconstruction. Per particle CTF and motion correction were performed followed by 3D auto-refinement with I1 symmetry resulted in an unmasked structure at 2.55 Å. Masking resulted in a final resolution of 2.36 Å (gold-standard $FSC_{0.143}$).

Model building and structure refinement.

A preliminary model for native AAVGo.1 was generated using the native AAVGo.1 VP3 protein sequence threaded into the 2.1 Å AAV5 structure (PDBid: 7kp3) in Coot (27). The starting model for the PKD1 domain of the receptor came from the 2.5 Å AAV5:PKD1-2 structure (PDBid: 7kpn). The models and imaging parameters were refined using RSRef 0.5.6 (28) with a final real-space correlation coefficient (CC) of 0.87 for native AAVGo.1 and 0.83 for complexed AAVGo.1:PKD1. (Correlation coefficients were calculated using all map grid points within 2.0 and 2.4 Å of all atoms, respectively.) Manual model adjustments were executed in Coot 0.8.9.2.

ACKNOWLEDGMENTS

The Chapman lab is grateful for the contributions of the University of Missouri Electron Microscopy Core the Purdue Cryo-EM Facility. Thank you also to Dr. Jianming Qiu and Dr. David Pintel for AAVGo.1 and AAV5 Rep-Cap plasmids. This work supported by the National Institute of Health R35 GM122564. Purdue Cryo-EM Facility data acquisition was supported by National Institute of General Medical Sciences Grant U24 GM116789. Atomic models and cryo-EM maps will be made available at the PDB and EMDB.

REFERENCES

1. Berns KI, Muzyczka N. 2017. AAV: An Overview of Unanswered Questions. Hum Gene Ther 28:308-313.
2. Xie Q, Bu W, Bhatia S, Hare J, Somasundaram T, Azzi A, Chapman MS. 2002. The atomic structure of adeno-associated virus (AAV-2), a vector for human gene therapy. Proc Natl Acad Sci U S A 99:10405-10.
3. Berns KI, Giraud C. 1996. Biology of adeno-associated virus. Curr Top Microbiol Immunol 218:1-23.
4. Meyer NL, Chapman MS. 2021. Adeno-associated virus (AAV) cell entry: structural insights. Trends Microbiol doi:10.1016/j.tim.2021.09.005.
5. Large EE, Silveria MA, Zane GM, Weerakoon O, Chapman MS. 2021. Adeno-Associated Virus (AAV) Gene Delivery: Dissecting Molecular Interactions upon Cell Entry. Viruses 13.
6. Pillay S, Meyer NL, Puschnik AS, Davulcu O, Diep J, Ishikawa Y, Jae LT, Wosen JE, Nagamine CM, Chapman MS, Carette JE. 2016. An essential receptor for adeno-associated virus infection. Nature 530:108-12.
7. Poon MW, Tsang WH, Chan SO, Li HM, Ng HK, Waye MM. 2011. Dyslexia-associated kiaa0319-like protein interacts with axon guidance receptor nogo receptor 1. Cell Mol Neurobiol 31:27-35.
8. Zhang R, Cao L, Cui M, Sun Z, Hu M, Zhang R, Stuart W, Zhao X, Yang Z, Li X, Sun Y, Li S, Ding W, Lou Z, Rao Z. 2019. Adeno-associated virus 2 bound to its cellular receptor AAVR. Nature Microbiology 4:675-682.
9. Zhang R, Xu G, Cao L, Sun Z, He Y, Cui M, Sun Y, Li S, Li H, Qin L, Hu M, Yuan Z, Rao Z, Ding W, Rao Z, Lou Z. 2019. Divergent engagements between adeno-associated viruses with their cellular receptor AAVR. Nat Commun 10:3760.
10. Meyer N, Davulcu O, Xie Q, Silveria M, Zane G, Large E, Chapman M. 2020. Expression and Purification of Adeno-associated Virus Virus-like Particles in a

Baculovirus System and AAVR Ectodomain Constructs in E. coli. Bio-Protocol 10:e3513.

11. Silveria MA, Large EE, Zane GM, White TA, Chapman MS. 2020. The Structure of an AAV5-AAVR Complex at 2.5 A Resolution: Implications for Cellular Entry and Immune Neutralization of AAV Gene Therapy Vectors. Viruses 12:1326.
12. Meyer NL, Hu G, Davulcu O, Xie Q, Noble AJ, Yoshioka C, Gingerich DS, Trzynka A, David L, Stagg SM, Chapman MS. 2019. Structure of the gene therapy vector, adeno-associated virus with its cell receptor, AAVR. Elife 8:e44707.
13. Pillay S, Zou W, Cheng F, Puschnik AS, Meyer NL, Ganaie SS, Deng X, Wosen JE, Davulcu O, Yan Z, Engelhardt JF, Brown KE, Chapman MS, Qiu J, Carette JE. 2017. Adeno-associated Virus (AAV) Serotypes Have Distinctive Interactions with Domains of the Cellular AAV Receptor. J Virol 91:e00391-17.
14. Dudek AM, Pillay S, Puschnik AS, Nagamine CM, Cheng F, Qiu J, Carette JE, Vandenberghe LH. 2018. An Alternate Route for Adeno-associated Virus (AAV) Entry Independent of AAV Receptor. J Virol 92.
15. Hu G, Silveria MA, Chapman MS, Stagg SM. 2022. Adeno-associated Virus Receptor-binding: Flexible Domains and Alternative Conformations through cryo-Electron Tomography of AAV2 and AAV5 complexes. bioRxiv doi:10.1101/2022.01.10.475736:2022.01.10.475736.
16. Qiu J, Cheng F, Pintel D. 2006. Molecular characterization of caprine adeno-associated virus (AAV-Go.1) reveals striking similarity to human AAV5. Virology 356:208-16.
17. Arbetman AE, Lochrie M, Zhou S, Wellman J, Scallan C, Doroudchi MM, Randlev B, Patarroyo-White S, Liu T, Smith P, Lehmkuhl H, Hobbs LA, Pierce GF, Colosi P. 2005. Novel caprine adeno-associated virus (AAV) capsid (AAV-Go.1) is closely related to the primate AAV-5 and has unique tropism and neutralization properties. J Virol 79:15238-45.
18. Govindasamy L, DiMattia MA, Gurda BL, Halder S, McKenna R, Chiorini JA, Muzyczka N, Zolotukhin S, Agbandje-McKenna M. 2013. Structural insights into adeno-associated virus serotype 5. J Virol 87:11187-99.
19. Chapman MS, Liljas L. 2003. Structural folds of viral proteins. Adv Protein Chem 64:125-96.
20. Tsao J, Chapman MS, Agbandje M, Keller W, Smith K, Wu H, Luo M, Smith TJ, Rossmann MG, Compans RW, et al. 1991. The three-dimensional structure of canine parvovirus and its functional implications. Science 251:1456-64.
21. Govindasamy L, Padron E, McKenna R, Muzyczka N, Kaludov N, Chiorini JA, Agbandje-McKenna M. 2006. Structurally mapping the diverse phenotype of adeno-associated virus serotype 4. J Virol 80:11556-70.
22. Jose A, Mietzsch M, Smith JK, Kurian J, Chipman P, McKenna R, Chiorini J, Agbandje-McKenna M. 2019. High-Resolution Structural Characterization of a New Adeno-associated Virus Serotype 5 Antibody Epitope toward Engineering Antibody-Resistant Recombinant Gene Delivery Vectors. J Virol 93.
23. Suloway C, Pulokas J, Fellmann D, Cheng A, Guerra F, Quispe J, Stagg S, Potter CS, Carragher B. 2005. Automated molecular microscopy: the new Leginon system. J Struct Biol 151:41-60.

24. Zivanov J, Nakane T, Forsberg BO, Kimanius D, Hagen WJ, Lindahl E, Scheres SH. 2018. New tools for automated high-resolution cryo-EM structure determination in RELION-3. Elife 7.
25. Rohou A, Grigorieff N. 2015. CTFFIND4: Fast and accurate defocus estimation from electron micrographs. J Struct Biol 192:216-21.
26. Zheng SQ, Palovcak E, Armache JP, Verba KA, Cheng Y, Agard DA. 2017. MotionCor2: anisotropic correction of beam-induced motion for improved cryo-electron microscopy. Nat Methods 14:331-332.
27. Emsley P, Lohkamp B, Scott WG, Cowtan K. 2010. Features and development of Coot. Acta Crystallogr D Biol Crystallogr 66:486-501.
28. Chapman MS, Trzynka A, Chapman BK. 2013. Atomic modeling of cryo-electron microscopy reconstructions--joint refinement of model and imaging parameters. J Struct Biol 182:10-21.

342 **FIGURES**

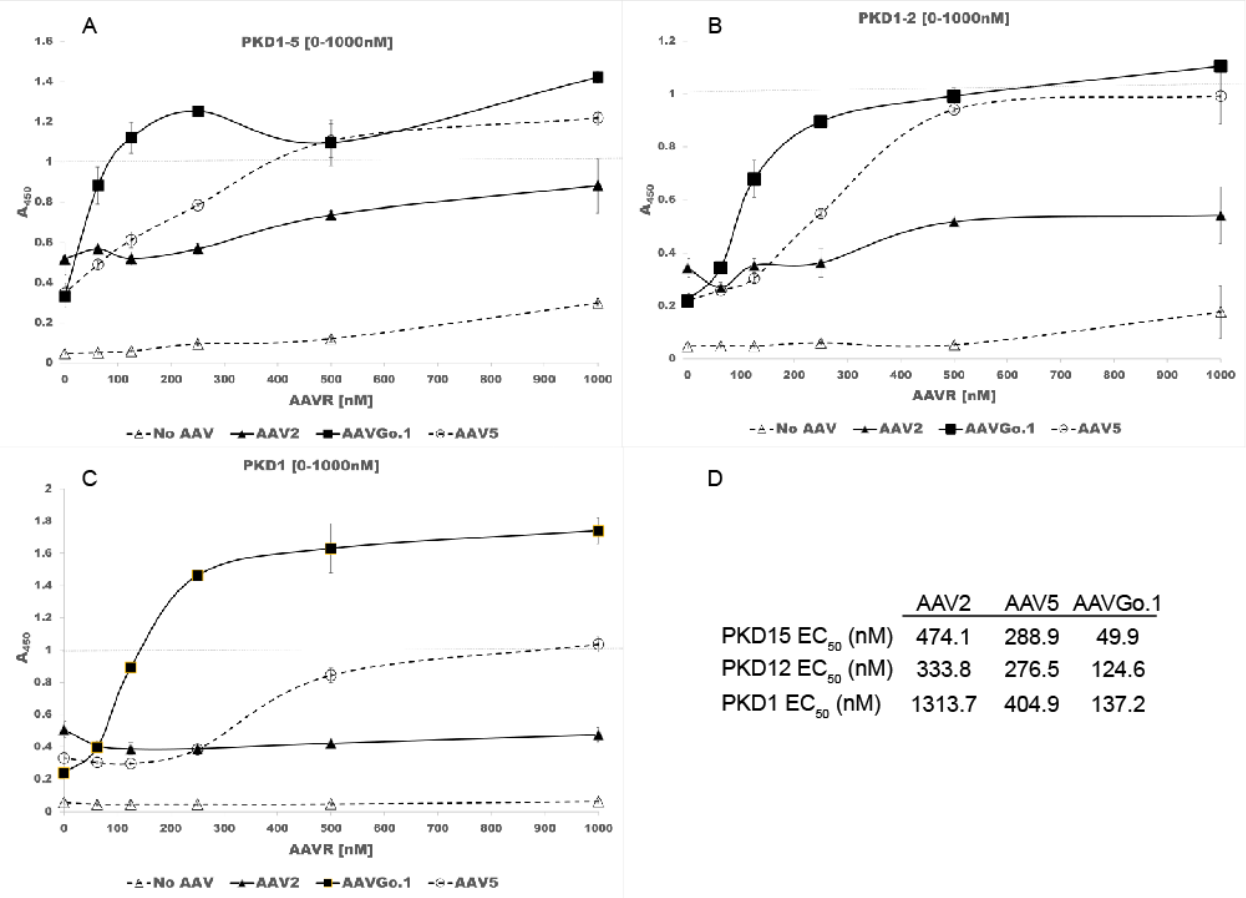

D

	AAV2	AAV5	AAVGo.1
PKD15 EC_{50} (nM)	474.1	288.9	49.9
PKD12 EC_{50} (nM)	333.8	276.5	124.6
PKD1 EC_{50} (nM)	1313.7	404.9	137.2

344 *Figure 1: AAVGo.1 interacts with PKD domains. A) PKD15 ELISA. B) PKD12 ELISA. C)*

345 *PKD1 ELISA. D) EC_{50} values determined from panels A-C.*

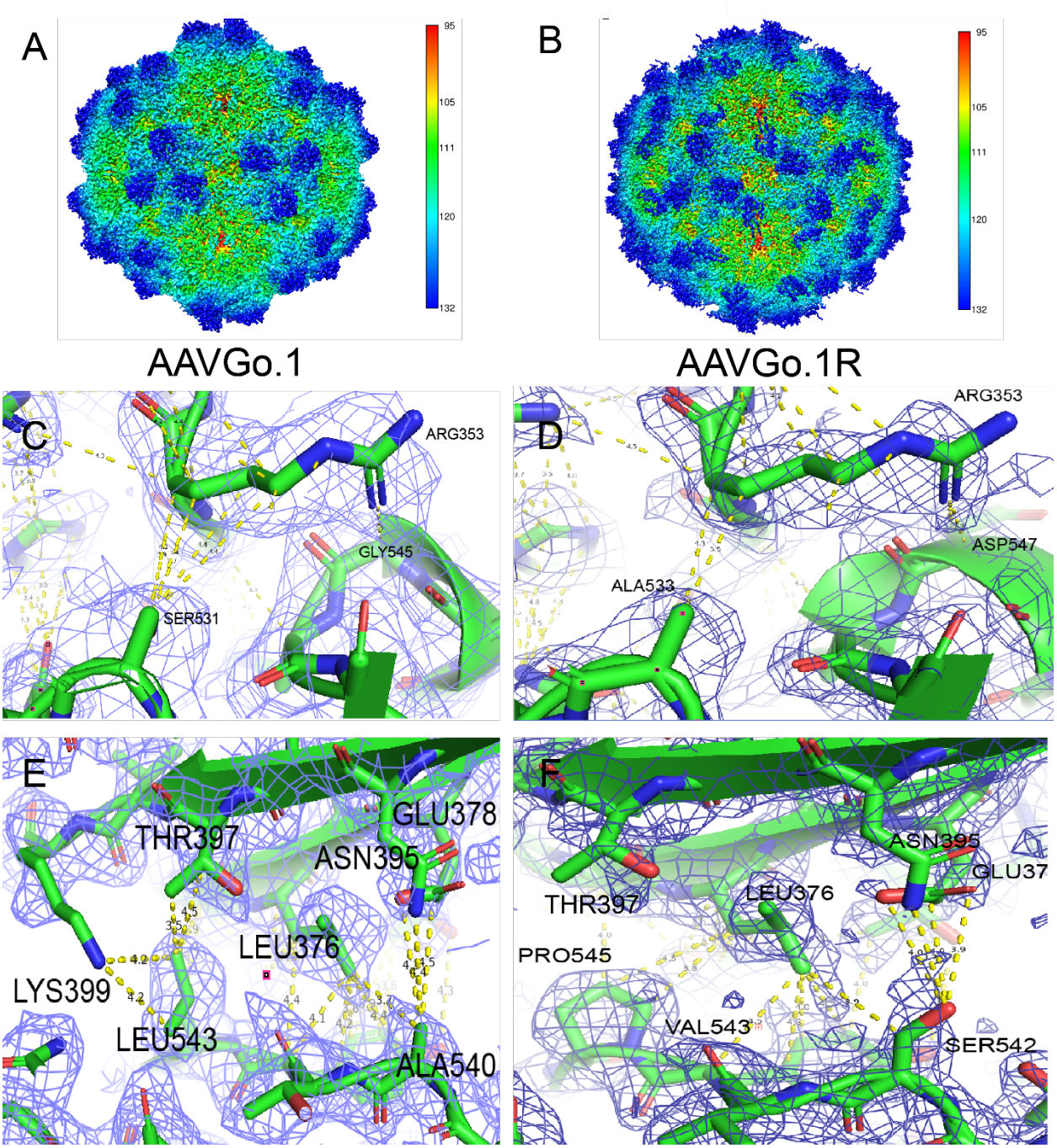

347 *Figure 2: The receptor site on AAVGo is similar to AAV5 with some key differences. A)*

348 *Native reconstruction of AAVGo.1, colored by distance from the virus center. B)*

349 *AAVGo.1 complexed with PKD1. The AAV5 PKD1 N-terminus begins above the edge of*

350 *the 5-fold pore and descends towards the 2-fold axis (Silveria, Large et al. 2020).*

Panels C – E together show the environment for the four interface residues that differ between AAV5 (left) and AAVGo.1 (right). Atomic models are overlaid on maps contoured at 1.5 σ. C) The AAV5 environment around AAVR-Arg$_{353}$, AAV5-Ser$_{531}$ and AAV5-Gly$_{545}$. D) The corresponding AAVGo.1 environment around huAAVR-Arg$_{353}$, AAVGo.1-Ala$_{533}$ and AAVGo.1-Asp$_{547}$. E) The AAV5 environment around Leu$_{543}$ and Ala$_{540}$. D) The corresponding AAVGo.1 environment around Pro$_{545}$ and Ser$_{542}$.

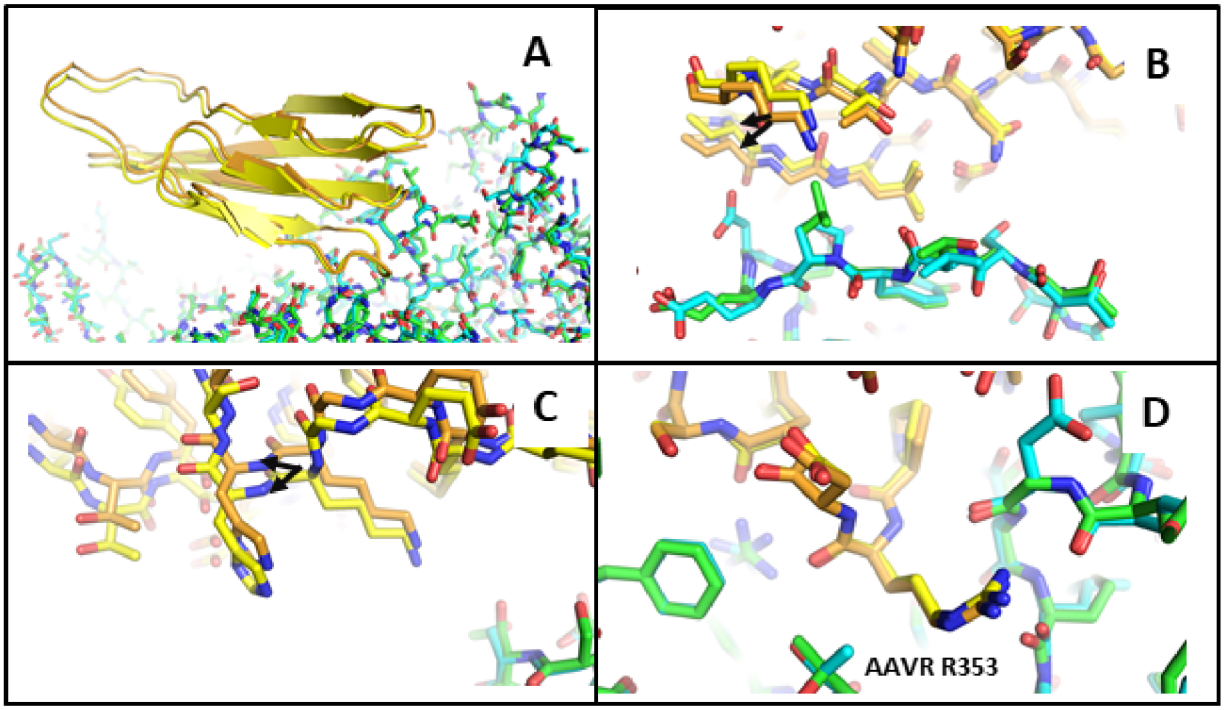

Figure 3: A rotation in the PKD1 position is observed when comparing its bound structure to AAVGo.1 versus AAV5. AAVGo.1 is colored with cyan carbons while AAV5 is colored with green carbons. The PKD1 from the AAVGo.1 structure is colored with yellow carbons and the PKD1 from the AAV5 structure is colored with orange carbons. A) The overall rotation is observed in the PKD1 position when bound to either AAVGo.1 or AAV5. B) A close up shows the PKD1-viral interface near AAVR Lys_{399}. Arrows indicate a pair of corresponding atoms that differ by ~1 Å. C) This view is near AAVR His_{363}. D) On the lowermost turn in panel A, AAVR Arg_{353} is bound more closely in a pocket on the AAV surface, and there is little difference between AAVGo.1 and AAV5. Thus the overall displacement is approximately a rotation about an R353 pivot point.

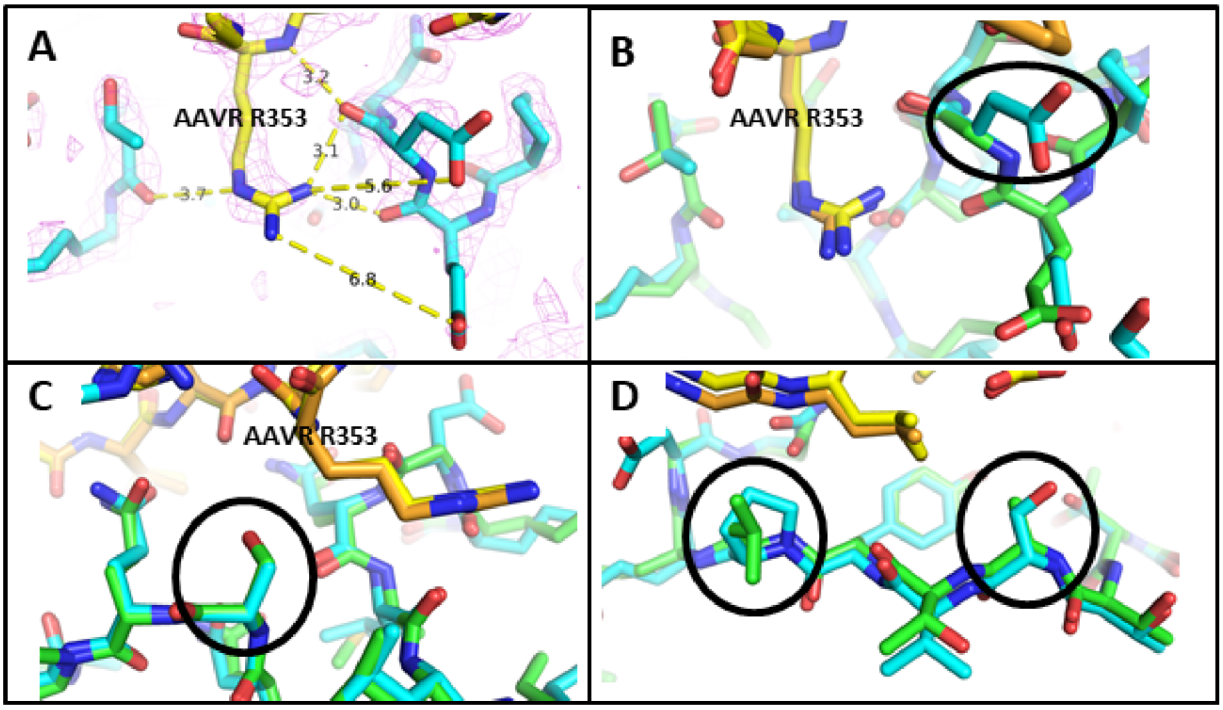

Figure 4: Comparison of the virus-receptor complexes of AAVGo.1 with AAV5. A) AAVR (yellow carbons) bound to AAVGo.1 (cyan carbons) near AAVR-Arg$_{353}$. B) The AAV5 complex structure (PDBid 7kpn) is overlaid with green / orange carbon atoms. Circled are the substitutions of Asp$_{547}$ for Gly$_{545}$ in AAVGo.1 (vs. AAV5) providing a more complementary, negatively charged binding pocket for AAVR-Arg$_{353}$. C) Circled is the substitution of AAVGo.1 Ala$_{533}$ for AAV5 Ser$_{531}$. D) Within the circles, Pro$_{545}$ and Asp$_{547}$ replace AAV5 residues Leu$_{543}$ and Gly$_{545}$.

376 **TABLES**

377 *Table 1: Cryo-EM data acquisition and processing*

Data Collection	**AAVGo.1**	**AAVGo.1R**
Magnification (x)	64,000	64,000
Voltage (kV)	300	300
Electron Exposure (e/Å^2)	35.4	32.9
Defocus Range (μm)	-0.7 to -2.0	-0.7 to -2.0
Pixel Size (Å)	0.664	0.664
Data Processing		
Motion Correction	Relion 3.1.1	Relion 3.1.1
CTF Estimation	CTFFIND-4.1	CTFFIND-4.1
Symmetry Imposed	I1	I1
Initial Particle Images	246,094	208,921
Final Particle Images	140,568	71,095
Map Resolution	2.93	2.36
FSC Threshold	0.143	0.143

378

379